scientific reports

Check for updates

OPEN

Impact of *hcp* and *vgrG* on *Acinetobacter baumannii* biofilm formation during infection of human pulmonary alveolar epithelial cells

Meiyuan Huang[1], Mengting Liu[1], Wenjie Yang[1], Pinqiong Qin[1], Yueqi Zhang[1] & Daojun Yu[1,2]✉

The purpose of this research is to examine the impact of key type VI secretion system (T6SS) proteins hemolysin coregulated protein (Hcp) and valine-glycine repeat protein G (VgrG) on the metabolism of *Acinetobacter baumannii* (*A. baumannii*). Homologous recombination technology was used to construct *hcp* knockout strain (ATCC17978Δ*hcp*), *vgrG* knockout strain (ATCC17978Δ*vgrG*), and a combined *hcp* and *vgrG* knockout strain (ATCC17978Δ*hcp*Δ*vgrG*), with the wild-type *A. baumannii* strain (ATCC17978) used as a control. These strains were co-cultured with human pulmonary alveolar epithelial cells (HPAEpiC), respectively. Subsequently, a non-targeted metabolomic analysis of the co-culture supernatant, bacteria, and cells was conducted using liquid chromatography-tandem mass spectrometry (LC-MS/MS). In the bacterial three-pair comparison groups, the major differential metabolites were organic acids and derivatives, as well as organic oxygen compounds ($p < 0.05$). Further analysis of the major differential metabolites in bacteria revealed five common metabolites with statistically significant differences ($p < 0.05$), which were N-acetyl-d-glucosamine 6-phosphate, 6-hydroxypseudooxynicotine, 3-deoxy-D-manno-octulosonate, N-Acetylneuraminic acid, and N-acetylmuramoyl-Ala. The annotation of the above five differential metabolites identified five common metabolic pathways with statistically significant differences ($p < 0.05$). Among these, phosphotransferase system (PTS) showed significant statistical differences ($p = 0.01$, $p = 0.04$, $p = 0.03$) in ATCC17978Δ*hcp*, ATCC17978Δ*vgrG*, and ATCC17978Δ*hcp*Δ*vgrG*. The deletion of *hcp* and the combined deletion of *hcp* and *vgrG* led to a downregulation of PTS overall expression, while the deletion of *vgrG* did not show a significant change in the overall expression level of PTS. The PTS shows a correlation with biofilm formation. The validation experiments demonstrated that ATCC17978Δ*hcp* exhibited significant phenotypic defects, including reduced biofilm formation capacity and visible surface damage under scanning electron microscopy (SEM). In contrast, ATCC17978Δ*vgrG* maintained wild-type levels of biofilm formation and intact bacterial morphology. Notably, ATCC17978Δ*hcp*Δ*vgrG* displayed a unique phenotypic reversal, characterized by enhanced biofilm formation, intact bacterial structure, and increased extracellular polymeric substance (EPS) secretion. However, all mutant strains exhibited decreased adhesion ability. The expression levels of biofilm-related genes in each strain showed a positive correlation with their biofilm formation capacity. These results demonstrate that while the PTS influences biofilm formation, it does not serve as the sole regulatory mechanism. The *hcp* gene plays a crucial role in biofilm formation, whereas the *vgrG* gene exhibits minimal impact on biofilm formation. Their co-deletion triggers compensatory pathways enhancing biofilm production.

Keywords *Acinetobacter baumannii*, Hemolysin co-regulated protein, Valine-glycine repeat protein G, Type VI secretion system, Phosphotransferase system, Biofilm

[1]The Fourth School of Clinical Medicine, Zhejiang Chinese Medical University, Hangzhou First People's Hospital, Hangzhou, China. [2]Affiliated Hangzhou First People's Hospital, School of Medicine, Westlake University, Hangzhou, China. ✉email: yudaojun@hospital.westlake.edu.cn

Acinetobacter baumannii (*A. baumannii*) is one of the common opportunistic pathogens that can cause widespread and severe nosocomial infections, which are especially fatal in immunocompromised patients who have underlying diseases or have undergone major surgery[1]. *A. baumannii* can exert virulence through membrane porin[2], capsular polysaccharide[3], phospholipase[4], outer membrane vesicles[5], iron acquisition systems[6] and protein secretion systems[7].

The protein secretion system is a crucial virulence factor in *A. baumannii*. Currently, four types of secretion systems have been found in *A. baumannii*: type I secretion system (T1SS), type II secretion system (T2SS), type V secretion system (T5SS), and type VI secretion system (T6SS)[8]. These secretion systems not only transport virulence factors to the surrounding environment or directly transfer them to adjacent cells, [9]but also hold significant importance in antibacterial resistance[10]. Among these, the T6SS is capable of directly injecting toxic effector molecules into the cells of both prokaryotic and eukaryotic hosts[11], thereby playing a crucial role in interactions between bacteria and their hosts[12]. The structure of the T6SS resembles a contractile bacteriophage tail device. Hemolysin co-regulated protein (Hcp), valine-glycine repeat protein G (VgrG), proline-alanine-alanine-arginine (PAAR), TssB and TssC form the phage-like tail tube, tail spike and sheath components, respectively, which together form the tube-sheath complex of the T6SS. Hcp is a hexameric tubular structure characterised by helical symmetry, capable of carrying effector molecules and interacting with substrates[13]. VgrG, a trimeric structure located at the tip of the tail tube, is sharpened by the conical PAAR protein, which facilitates the secretion of effector proteins[14]. TssB and TssC form a contractile sheath that provides the energy required for the transport of effector proteins[15]. As Hcp and VgrG are released into the extracellular environment after activation of the system, they can serve as molecular markers of T6SS activity[16,17].

Metabolomics enables the comprehensive and systematic analysis of all small molecule metabolites in an organism, thereby identifying the role of specific metabolites in disease and searching for biomarkers of disease onset, progression and severity[18]. Metabolomics can be divided into targeted and untargeted analytical approaches. Untargeted metabolomics has been widely applied in bacterial research and has proven to be a successful research method. In terms of bacterial virulence, studies have shown that key secondary metabolites linked to virulence, including rhamnolipids, alkyl quinolones, and phenazines, are notably elevated in highly virulent strains of *Pseudomonas aeruginosa*. Furthermore, a predictive model for distinguishing between *Pseudomonas aeruginosa* strains has been developed by integrating metabolite features with machine learning[19]. In terms of bacterial-host interactions, Nicole Aiosa and colleagues studied the changes in the metabolome of *Burkholderia thailandensis* co-cultured with mammalian host cells and identified the roles of infection-related metabolites in bacterial virulence and host defence, providing new insights for in-depth analysis of bacterial-host interactions[20]. In addition, untargeted metabolomics can also be used to study biofilms, bacterial stress responses and environmental adaptation[21,22].

However, there remains a scarcity in untargeted metabolomics research on *A. baumannii*. Therefore, further exploration of *A. baumannii*'s metabolite profile, metabolic pathways, and their associations with virulence, antibiotic resistance, and other factors holds significant academic and clinical value.

In this study, we constructed ATCC17978Δ*hcp*, ATCC17978Δ*vgrG*, and ATCC17978Δ*hcp*Δ*vgrG*, with the wild-type *A. baumannii* strain (ATCC17978) used as a control. We performed untargeted identification and differential comparison of metabolites in different *A. baumannii* strains using liquid chromatography-tandem mass spectrometry (LC-MS/MS) to investigate the effects of key T6SS genes *hcp* and *vgrG* on the metabolic activity of *A. baumannii*.

Methods

Bacterial strains, cells and growth conditions

A. baumannii strain ATCC17978 was kindly provided by Sir Run Run Shaw Hospital, affiliated with the Zhejiang University School of Medicine. The mutant strains ATCC17978Δ*hcp*, ATCC17978Δ*vgrG*, and ATCC17978Δ*hcp*Δ*vgrG* were constructed in our laboratory using homologous recombination technology. Human pulmonary alveolar epithelial cells (HPAEpiC) were purchased from Wuhan Saios Biotechnology Co., Ltd.

A. baumannii was cultured in Luria–Bertani (LB) broth or on blood agar plates at 37 °C. HPAEpiC were cultured in specialized epithelial cell medium supplemented with 2% fetal bovine serum (FBS) and 1% penicillin-streptomycin (100 μg/mL each) at 37 °C under 5% CO_2.

Non-targeted metabolomics analysis

HPAEpiC were seeded in culture flasks and cultured in antibiotic-containing medium until reaching 80–90% confluence, followed by replacement with serum- and antibiotic-free medium. Concurrently, four strains of *A. baumannii* were cultured overnight in LB broth, harvested by centrifugation, and resuspended in serum- and antibiotic-free epithelial cell medium. Based on the preliminary real-time cell analysis (RTCA) experimental results from our research group (a sharp decrease in growth index after 12 h of co-culture), a bacterial suspension with a multiplicity of infection (MOI) of 100:1 was used for co-culturing with HPAEpiC for 12 h. After co-culture, the culture medium was collected and centrifuged at 2,000 rpm for 10 min to harvest a portion of the cell pellet. Subsequently, the sample was centrifuged at 13,000 rpm for 10 min to collect the bacterial pellet. Meanwhile, the co-culture supernatant was filtered through a 0.22 μm membrane to obtain it. The adherent cells were treated with trypsin and then centrifuged at 2,000 rpm for 10 min to collect the remaining cell pellet. All samples were divided into nine comparison groups (Table 1), and subjected to non-targeted metabolomics analysis by Mingke Biotechnology Co., Ltd. (Hangzhou, China).

LC-MS/MS was performed using a Waters Acquity I-Class PLUS UPLC system coupled with an Xevo G2-XS QToF high-resolution mass spectrometer, equipped with a UPLC HSS T3 column (1.8 μm, 2.1 × 100 mm). Mass spectral data were acquired in MSe mode under the control of MassLynx V4.2 software, enabling simultaneous

Components	Comparison groups		
Supernatant	SH vs. SWT	SV vs. SWT	SHV vs. SWT
Bacteria	ABH vs. ABWT	ABV vs. ABWT	ABHV vs. ABWT
Cells	CH vs. CWT	CV vs. CWT	CHV vs. CWT

Table 1. Metabolite comparison of different co-culture groups.

dual-channel data acquisition at low and high collision energies. Raw data were processed using Progenesis QI software for peak extraction, alignment, and preprocessing, with metabolite annotation conducted against the METLIN online database, public databases, and a custom database.

Bioinformatic analyses were performed in R. Principal component analysis (PCA) utilized the prcomp package, while orthogonal partial least squares-discriminant analysis (OPLS-DA) was implemented via the ropls package[23]. Volcano plots were generated using ggplot2[24]. Metabolites were annotated and classified based on the Human Metabolome Database (HMDB)[25]and pathway enrichment analysis was conducted using the Kyoto Encyclopedia of Genes and Genomes (KEGG)[26,27].

For statistical analysis, univariate analysis employed Student's t-test and fold change (FC) to evaluate the significance of differential metabolites. Multivariate analysis included unsupervised PCA and supervised OPLS-DA. Metabolites with variable importance in projection (VIP) scores > 1 and $p < 0.05$ in the OPLS-DA model were considered statistically significant.

S/AB/C represent the supernatant, bacterial component, and cell component from the co-culture system, respectively. WT/H/V/HV represent ATCC17978, ATCC17978Δ*hcp*, ATCC17978Δ*vgrG*, and ATCC17978Δ*hcp*Δ*vgrG*, respectively.

Biofilm assay

Biofilm quantification was performed using the crystal violet microplate assay[28]. The collected *A. baumannii* strains that had been co-cultured with HPAEpiC were resuscitated on blood agar plates. Fresh single colonies were then suspended in sterile saline to achieve 0.5 McFarland turbidity, followed by 1:100 dilution in LB broth. Aliquots of 200 µL were dispensed into 96-well plates with three replicates per strain and incubated statically at 37 °C for 24 h. After aspirating the bacterial cultures, wells were gently washed with PBS to remove planktonic bacteria, air-dried, and fixed with methanol for 10 min. Biofilms were stained with 200 µL of 0.1% crystal violet for 10 min, washed with PBS to remove excess stain, and air-dried again. Finally, the bound dye was solubilized with 200 µL of 95% ethanol, and absorbance was measured at 570 nm using a microplate reader to quantify biofilm formation.

Scanning electron microscopy (SEM)

The collected *A. baumannii* strains that had been co-cultured with HPAEpiC were individually inoculated into LB broth and cultured overnight at 37 °C with shaking at 180 rpm. Bacteria were harvested by centrifugation and washed twice with PBS. Subsequently, the samples were fixed overnight at 4 °C in a 2.5% glutaraldehyde solution and washed three times (15 min each) with 0.1 M phosphate buffer (pH 7.0). The samples were then subjected to gradient dehydration by sequential immersion in 50%, 75%, and 90% ethanol solutions for 10 min each, followed by three immersions (10 min each) in 100% anhydrous ethanol. The ethanol was then replaced by sequential immersion in 50%, 75%, and 90% t-butanol solutions for 10 min each, followed by three immersions (10 min each) in 100% t-butanol to remove residual ethanol. The processed samples were placed in small metal cups and stored at − 20 °C for later use. After freeze-drying, the samples were mounted on stubs with conductive carbon adhesive and sputter-coated with gold for 30 s using a Hitachi E1010 ion sputter. Finally, the samples were observed using a Hitachi SU8010 field-emission SEM.

Bacterial adherence assay

HPAEpiC were seeded in 24-well plates and cultured in epithelial cell medium containing dual antibiotics until reaching approximately 90% confluence, followed by replacement with serum- and antibiotic-free medium for subsequent experiments. Meanwhile, four strains of *A. baumannii* were individually inoculated into LB broth and cultured at 37 °C with shaking at 180 rpm for 18 h. The bacterial suspensions were adjusted to 0.5 McFarland standard, centrifuged, and resuspended in serum- and antibiotic-free medium. Based on previous RTCA (Real-Time Cell Analysis) results from our research group (showing the most significant growth index at 5 h of co-culture), HPAEpiC were co-cultured with each *A. baumannii* strain at an MOI of 100:1 for 5 h. After co-culture, the supernatant was discarded and cells were washed twice with PBS. Sterile distilled water was added to lyse the cells for 30 min, and the lysates were serially diluted and plated onto LB agar plates for overnight culture at 37 °C, followed by colony counting. Each experimental group was set up with three independent replicate wells. The bacterial adhesion rate was calculated using the formula: adhesion rate = (adherent bacterial count/inoculated bacterial count) ×100%.

Expression quantification by reverse transcription quantitative polymerase chain reaction (RT-qPCR)

The four strains of *A. baumannii* that had been co-cultured with HPAEpiC were resuscitated on blood agar plates. Subsequently, single colonies from each strain were individually inoculated into LB broth and cultured overnight at 37 °C with shaking at 180 rpm. After incubation, bacterial pellets were collected by centrifugation

at 12,000 rpm for 5 min. Total RNA was then extracted using the Modified Bacterial RNA Extraction Kit (SparkJade) following the manufacturer's instructions. The concentration of the extracted RNA was measured using the Nanodrop 2000 Nucleic Acid Analyzer (Thermo). Subsequently, cDNA was synthesized through reverse transcription using the HiScript III All-in-one RT SuperMix Perfect for qPCR kit (Vazyme) on a Model 9902 PCR machine (Applied Biosystems).

Specific primers targeting biofilm-associated genes of *A. baumannii* (including *bap*, *csuA*, *csuB*, *bfmS*, *bfmR*, *pgaA*, and *pgaD*) were designed based on sequence information obtained from the NCBI database, with *16 S rRNA* serving as the reference gene (Table 2). qPCR was performed using the ChamQ SYBR Color qPCR Master Mix kit (Vazyme) on an ABI 7500 Real-Time PCR System (Applied Biosystems). Relative changes in gene expression levels were calculated using the $2^{-\Delta\Delta Ct}$ method. To ensure experimental reproducibility and reliability, all procedures were performed with three biological replicates.

Results

Quality control data analysis

The base peak intensity (BPI) chromatograms of the seven quality control (QC) samples in this experiment show excellent overlap in peak retention times and peak areas, indicating good instrument stability (Supplementary Figure S1).

Multivariate statistical analysis of samples

Using unsupervised PCA, there was no overlap between the samples of different comparison groups, and they showed significant differences (Supplementary Figure S2). Based on these results, supervised OPLS-DA analyses were further performed. The R^2Y and Q^2Y values of the OPLS-DA models for each comparison group were both greater than 0.5 and close to 1, indicating good stability, fit, and predictive ability of the models. This made them suitable for screening differential metabolites and further reinforced the separation trends between the comparison groups, with more tightly concentrated distributions within each group (Supplementary Figure S3). The results of permutation tests indicated that the slope for the Q^2Y fitting regression line associated with each comparison group was positive, thus validating the statistical significance of the model. Additionally, all the blue points were located above the red points, indicative of a strong independence between the training and testing datasets utilized for the modeling process (Supplementary Figure S4). In conclusion, these results collectively indicate significant metabolic differences between the two sample groups in each comparison group.

Differential metabolite screening and identification

Metabolites were annotated and classified using HMDB, and those with VIP > 1 and $p < 0.05$ were selected as statistically significant differential metabolites[29]. In the comparative classification of differential metabolites, we will exclude the unclassified part.

Supernatant comparison groups

SH vs. SWT: In positive ion mode, we identified 229 differential metabolites, including 157 upregulated and 72 downregulated (Supplementary Figure S5A). These differential metabolites were classified into 10 groups, with lipids and lipid-like molecules constituting the largest proportion (14.41%) (Supplementary Figure S6A). In negative ion mode, we identified 305 differential metabolites, including 204 upregulated and 101 downregulated (Supplementary Figure S5B). These differential metabolites were classified into 9 groups, with organic acids and derivatives constituting the largest proportion (11.80%) (Supplementary Figure S6B).

SV vs. SWT: In positive ion mode, we identified 103 differential metabolites, including 67 upregulated and 36 downregulated (Supplementary Figure S5C). These differential metabolites were classified into 9 groups, with lipids and lipid-like molecules constituting the largest proportion (15.53%) (Supplementary Figure S6C). In negative ion mode, we identified 144 differential metabolites, including 84 upregulated and 60 downregulated

Genes	Primer Sequence (5'-3')	Product Size (bp)	Sources
bap	CCGATGGCGTAACTTTCTCG ATCAATCGCAACGCAAAACCA	232	This study
csuA	TTTTGGTGAAGCTACCACAGC ACCAGCACACTCGATCTGAAA	91	This study
csuB	TGCCTGCTACAACACCTACA GCCGCATGGGGTTCATTATT	198	This study
bfmR	TCTGCACCCATTTCCAGACC GTTTGTCGTGAAGTTCGCCC	101	This study
bfmS	TGCCATTTCATCGCTTCCCT CCGTTAGAGCGCAAAATCCG	102	This study
pgaA	AAGCAGCATTTTGAAGCGGG CCGGGATAGCTGCCATTGAT	102	This study
pgaD	CCGCAGCAAAGCTCCGAATA TCGAGTTAAATACCCCTGCTCA	92	This study
16S rRNA	TCGTGTCGTGAGATGTTGGG AGGGCCATGATGACTTGACG	142	This study

Table 2. The primers used in this study for detection of biofilm related genes.

(Supplementary Figure S5D). These differential metabolites were classified into 9 groups, with organic acids and derivatives constituting the largest proportion (12.50%) (Supplementary Figure S6D).

SHV vs. SWT: In positive ion mode, we identified 194 differential metabolites, including 151 upregulated and 43 downregulated (Supplementary Figure S5E). These differential metabolites were classified into 10 groups, with lipids and lipid-like molecules constituting the largest proportion (11.86%) (Supplementary Figure S6E). In negative ion mode, we identified 270 differential metabolites, including 202 upregulated and 68 downregulated (Supplementary Figure S5F). These differential metabolites were classified into 9 groups, with organic acids and derivatives constituting the largest proportion (12.96%) (Supplementary Figure S6F).

Bacterial comparison groups

ABH vs. ABWT: In positive ion mode, we identified 74 differential metabolites, including 58 upregulated and 16 downregulated (Fig. 1A). These differential metabolites were classified into 8 groups, with organic acids and derivatives and organic oxygen compounds both constituting the largest proportion (13.51%) (Fig. 2A). In negative ion mode, we identified 193 differential metabolites, including 153 upregulated and 40 downregulated (Fig. 1B). These differential metabolites were classified into 9 groups, with organic acids and derivatives constituting the largest proportion (11.92%) (Fig. 2B).

ABV vs. ABWT: In positive ion mode, we identified 52 differential metabolites, including 14 upregulated and 38 downregulated (Fig. 1C). These differential metabolites were classified into 7 groups, with organic oxygen compounds constituting the largest proportion (21.15%) (Fig. 2C). In negative ion mode, we identified 122 differential metabolites, including 50 upregulated and 72 downregulated (Fig. 1D). These differential metabolites were classified into 9 groups, with organic oxygen compounds constituting the largest proportion (13.11%) (Fig. 2D).

ABHV vs. ABWT: In positive ion mode, we identified 37 differential metabolites, including 21 upregulated and 16 downregulated (Fig. 1E). These differential metabolites were classified into 7 groups, with organic oxygen compounds constituting the largest proportion (21.62%) (Fig. 2E). In negative ion mode, we identified 111 differential metabolites, including 55 upregulated and 56 downregulated (Fig. 1F). These differential metabolites were classified into 9 groups, with organic acids and derivatives and organic oxygen compounds both constituting the largest proportion (11.71%) (Fig. 2F).

Cellular comparison groups

CH vs. CWT: In positive ion mode, we identified 107 differential metabolites, with 34 upregulated and 73 downregulated (Supplementary Figure S7A). These differential metabolites were classified into 9 groups, with

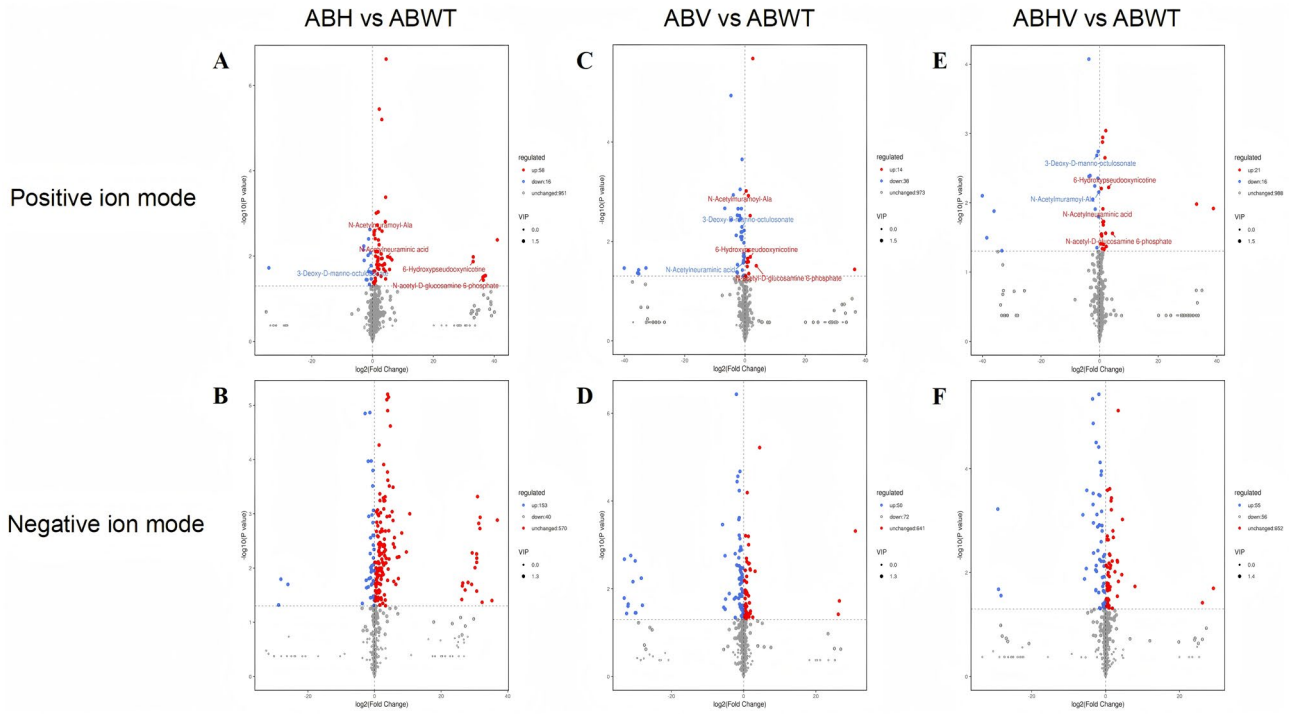

Fig. 1. Volcano plots of each comparison group in bacteria. In these plots, every point corresponds to a metabolite. The x-axis indicates the fold change in abundance across the groups being compared, while the y-axis illustrates the significance of the *p*-value. Larger points indicate higher VIP values. Downregulated differential metabolites are represented by blue points, upregulated differential metabolites are shown in red, and gray points signify metabolites that were identified but lacked significant differences. Additionally, five common differential metabolites were selected and labeled.

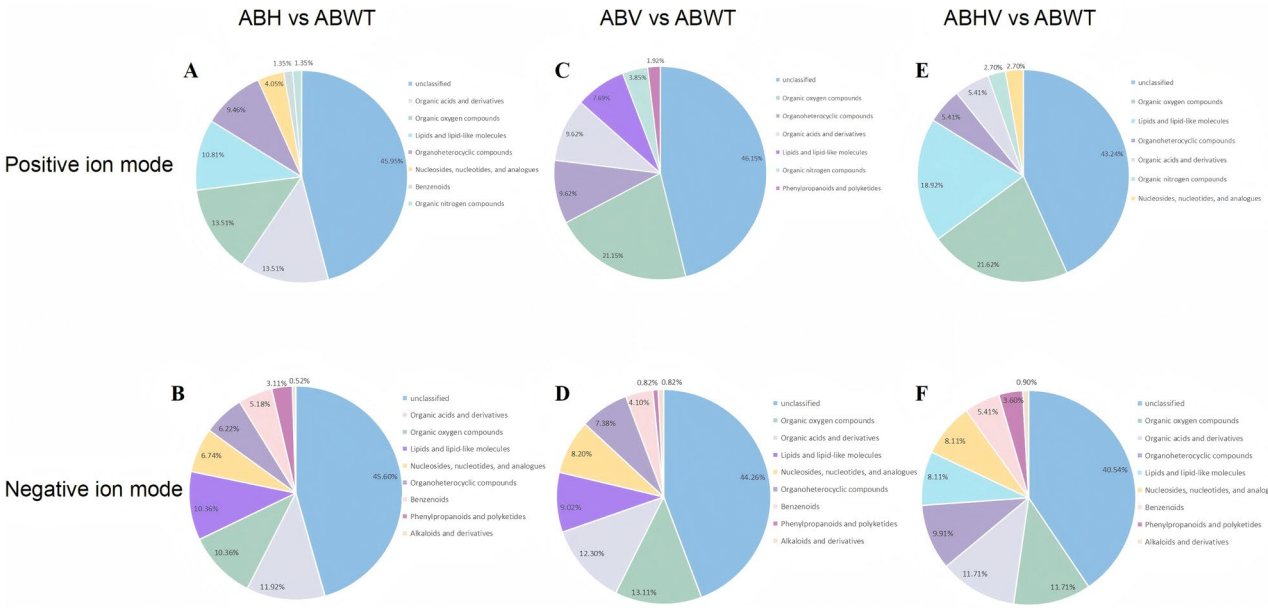

Fig. 2. Differential metabolite classification plots of each comparison group in bacteria.

lipids and lipid-like molecules constituting the largest proportion (14.02%) (Supplementary Figure S8A). In negative ion mode, we identified 209 differential metabolites, with 51 upregulated and 158 downregulated (Supplementary Figure S7B). These differential metabolites were classified into 9 groups, with organic acids and derivatives constituting the largest proportion (12.44%) (Supplementary Figure S8B).

CV vs. CWT: In positive ion mode, we identified 88 differential metabolites, with 54 upregulated and 34 downregulated (Supplementary Figure S7C). These differential metabolites were classified into 10 groups, with organic acids and derivatives and organoheterocyclic compounds both constituting the largest proportion (13.64%) (Supplementary Figure S8C). In negative ion mode, we identified 148 differential metabolites, with 90 upregulated and 58 downregulated (Supplementary Figure S7D). These differential metabolites were classified into 9 groups, with organic acids and derivatives constituting the largest proportion (14.86%) (Supplementary Figure S8D).

CHV vs. CWT: In positive ion mode, we identified 115 differential metabolites, with 30 upregulated and 85 downregulated (Supplementary Figure S7E). These differential metabolites were classified into 9 groups, with lipids and lipid-like molecules constituting the largest proportion (18.26%) (Supplementary Figure S8E). In negative ion mode, we identified 229 differential metabolites, with 52 upregulated and 177 downregulated (Supplementary Figure S7F). These differential metabolites were classified into 10 groups, with organic acids and derivatives constituting the largest proportion (13.54%) (Supplementary Figure S8F).

Differential metabolite KEGG enrichment analysis

Classification of the differential metabolites revealed a high degree of consistency between the major differential components of the supernatant and the cells. The subsequent pathway analysis will focus solely on the analysis of bacterial components.

In the comparisons of the bacterial components among the three groups, five common differential metabolites with statistical significance ($p < 0.05$) were identified from the most abundant organic acids and derivatives, as well as organic oxygen compounds. These metabolites are N-acetyl-d-glucosamine 6-phosphate, 6-hydroxypseudooxynicotine, 3-deoxy-D-manno-octulosonate, N-Acetylneuraminic acid, and N-acetylmuramoyl-Ala. Pathway annotation of these five metabolites using the KEGG database revealed five common differential metabolic pathways with statistical significance ($p < 0.05$): amino sugar and nucleotide sugar metabolism, O-antigen nucleotide sugar biosynthesis, phosphotransferase system (PTS), nicotinate and nicotinamide metabolism, and lipopolysaccharide biosynthesis. Among these, PTS showed significant statistical differences ($p = 0.01$, $p = 0.04$, $p = 0.03$) in ATCC17978Δ*hcp*, ATCC17978Δ*vgrG*, and ATCC17978Δ*hcp*Δ*vgrG* (Fig. 3). In the KEGG annotation pathway map and differential abundance score (DAS) plot of the PTS pathway, when comparing ATCC17978 with ATCC17978Δ*hcp* (ABH vs. ABWT), the expression of NAG-6P, β-Glucoside, and Fructose was upregulated in the wild-type strain, and the overall expression of PTS was upregulated (DAS = 0.43), indicating that the deletion of *hcp* leads to a downregulation of PTS expression (Figs. 4A and 5A). When comparing ATCC17978 with ATCC17978Δ*vgrG* (ABV vs. ABWT), NAG-6P expression was downregulated and β-Glucoside expression was upregulated in the wild-type strain, with no significant overall change in the PTS expression trend (DAS = 0), suggesting that the deletion of *vgrG* does not significantly affect PTS function (Figs. 4B and 5B). When comparing ATCC17978 with ATCC17978Δ*hcp*Δ*vgrG* (ABHV vs. ABWT), the expression of NAG-6P and Fructose was upregulated in the wild-type strain, and the overall

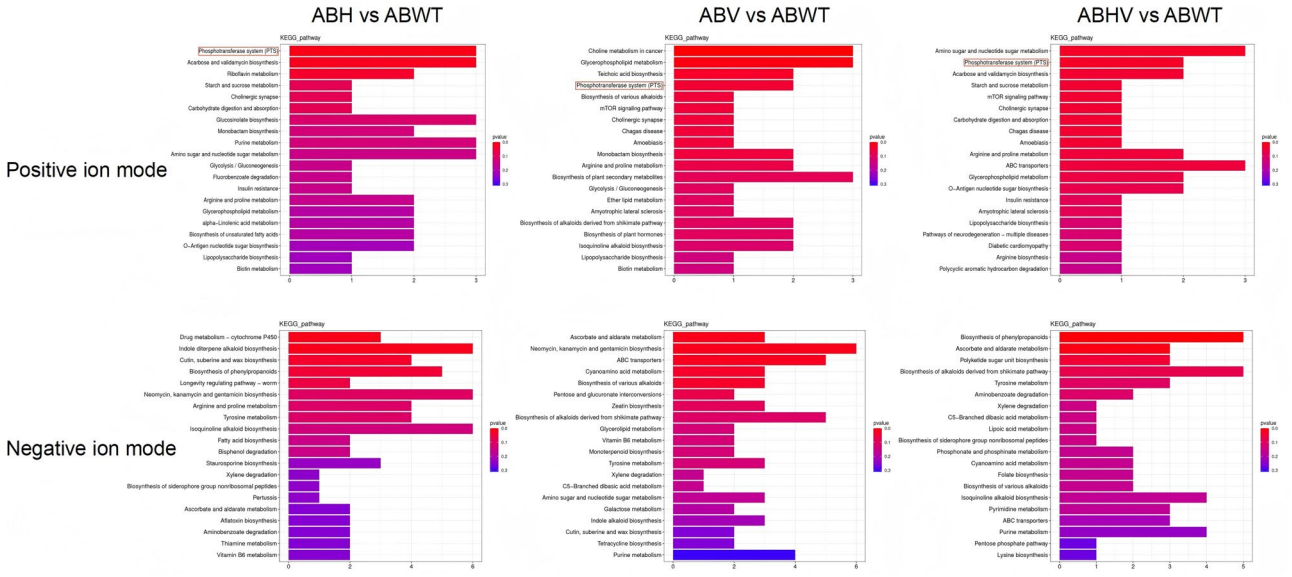

Fig. 3. Bar plots of pathway enrichment analysis for differential metabolites in each bacterial comparison group. The x-axis indicates the quantity of differential metabolites linked to each pathway, while the y-axis displays the names of these pathways. The intensity of the colors in the bar chart reflects the *P*-value, and the bars' lengths signify the number of metabolites associated with each pathway. PTS was marked with a red box.

expression of PTS was upregulated (DAS = 0.29), indicating that the combined deletion of *hcp* and *vgrG* leads to a downregulation of PTS expression (Figs. 4C and 5C).

Biofilm assay

Quantitative crystal violet staining revealed that compared to the wild-type strain, ATCC17978Δ*hcp* exhibited significantly reduced biofilm formation ($p < 0.01$), while ATCC17978Δ*vgrG* showed a non-significant decrease ($p > 0.05$). Notably, ATCC17978Δ*hcp*Δ*vgrG* demonstrated significantly enhanced biofilm-forming capacity ($p < 0.0001$) (Fig. 6).

SEM

The biofilm formation capacity of four *A. baumannii* strains was investigated using SEM at ×10,000 and ×30,000 magnifications. The results showed that all four strains maintained their typical rod-shaped morphology and aggregated to form clustered structures. The surface architecture of the wild-type strain was dense and uniform, with intact and plump bacterial morphology, resulting in structurally stable, continuous, and dense biofilms. The surface of ATCC17978Δ*hcp* exhibited varying degrees of damage, leading to loosely structured biofilms. ATCC17978Δ*vgrG* maintained relatively intact bacterial architecture, while ATCC17978Δ*hcp*Δ*vgrG* not only preserved complete morphological integrity but also secreted more abundant extracellular polymeric substances (EPS), forming structurally robust biofilms with significantly enhanced density (Fig. 7).

Bacterial adherence assay

The adhesion assay results demonstrated that compared to the wild-type strain, the adhesion ability of the three mutant strains decreased. However, the adhesion capacity of ATCC17978Δ*hcp*Δ*vgrG* was still stronger than that of ATCC17978Δ*hcp* and ATCC17978Δ*vgrG* (Fig. 8).

Expression quantification by RT-qPCR

Analysis of biofilm-related gene expression revealed that compared to the wild-type strain, ATCC17978Δ*hcp* exhibited a slight increase in *bfmS* expression but showed downregulation trends in other biofilm-related genes ($p > 0.05$). ATCC17978Δ*vgrG* demonstrated downregulation of *bap*, *csuB*, and *bfmR* genes alongside upregulation of *csuA*, *bfmS*, *pgaA*, and *pgaD* genes, with only the *csuA* expression change being statistically significant ($p < 0.01$). Consistent with the crystal violet biofilm assay results, all tested genes in ATCC17978Δ*hcp*Δ*vgrG* showed significantly elevated expression levels compared to the wild-type strain ($p < 0.05$) (Fig. 9).

Discussion

In this study, we found notable variations in metabolite expression among different *A. baumannii* gene knockout strains (ATCC17978Δ*hcp*, ATCC17978Δ*vgrG*, ATCC17978Δ*hcp*Δ*vgrG*) compared to the wild-type strain of *A. baumannii* (ATCC17978) during co-culture with HPAEpiC through non-targeted metabolomics analysis. In terms of the number of differential metabolites, our results suggest that supernatant > cells > bacteria, which is consistent with the characteristic that prokaryotes (*A. baumannii*) have weaker secretion capabilities compared to eukaryotes (HPAEpiC). Regarding the types of differential metabolites, the metabolism of lipids and lipid-like

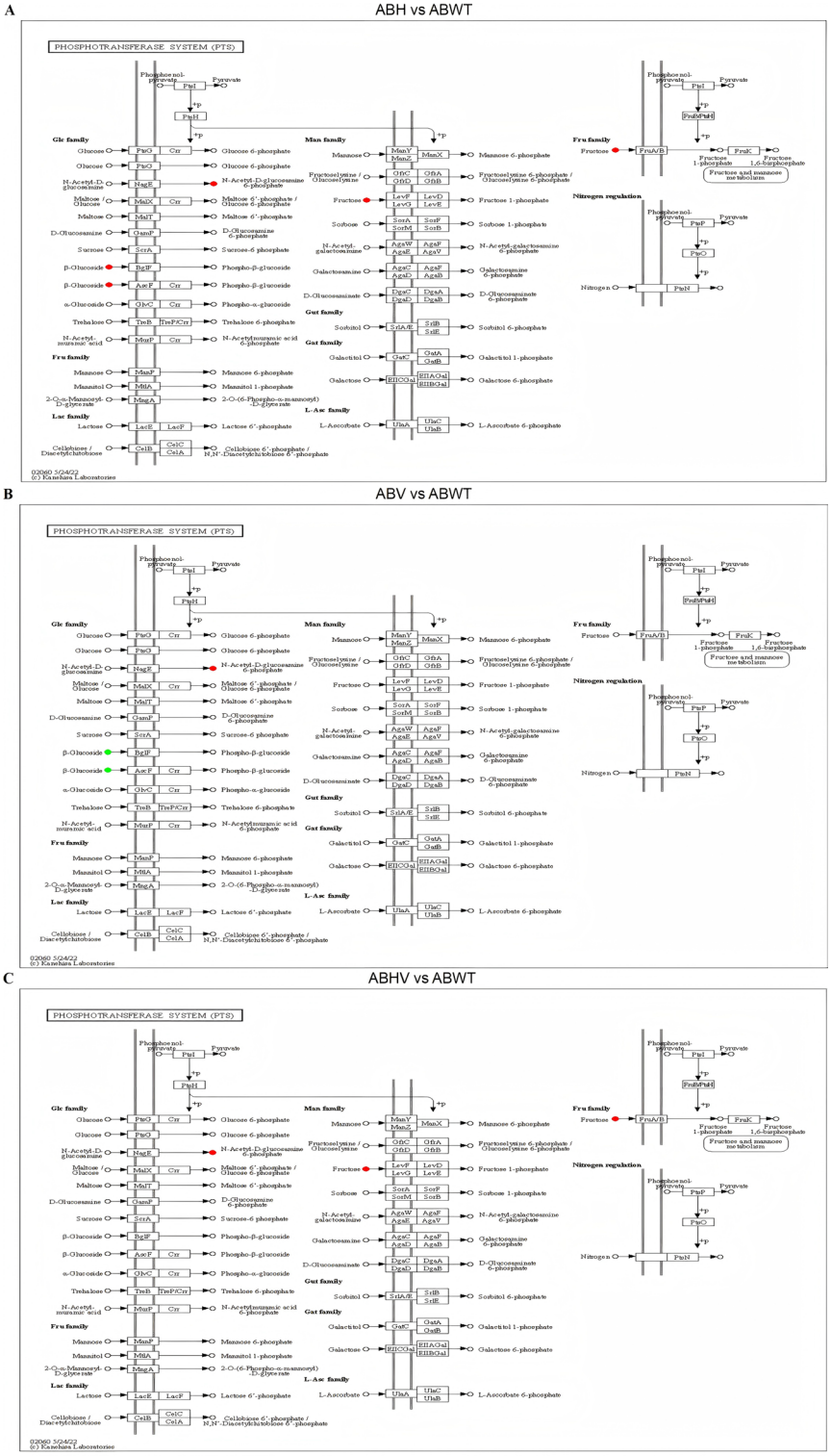

Fig. 4. KEGG annotation pathway maps of PTS in each bacterial comparison group. Red points indicate upregulation of metabolite content, while green points indicate downregulation of metabolite content. Adapted from KEGG pathway database (www.kegg.jp/kegg/kegg1.html).

molecules, as well as organic acids and their derivatives were predominantly affected in the supernatant and cellular triple-pair comparison groups. In the bacterial three-pair comparison groups, the metabolism of organic acids and their derivatives, as well as organic oxygen compounds, were predominantly affected. Although metabolites in the supernatant are co-secreted by both the bacteria and the cells, the amount of metabolites secreted by the cells was significantly higher than that secreted by the bacteria. Moreover, cell lysis leads to the

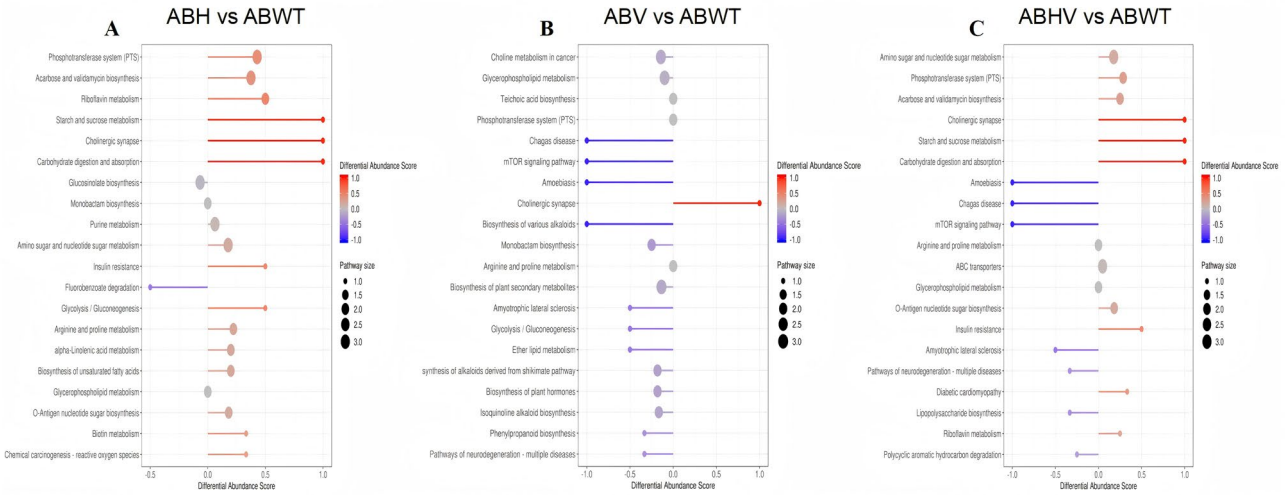

Fig. 5. DAS plots of each bacterial comparison group. The x-axis shows the DAS, while the y-axis depicts the names of pathways exhibiting differential expression. The lengths of the line segments correspond to the absolute values of the DAS, and the sizes of the circular markers indicate the quantity of differential metabolites within each pathway. The circular markers located on the left side of the axis indicate an overall downregulation tendency in the expression of this pathway. Conversely, the circular markers positioned on the right side of the axis signify an overall upregulation tendency in the pathway's expression. The color of the circles indicates the magnitude of the *p*-values.

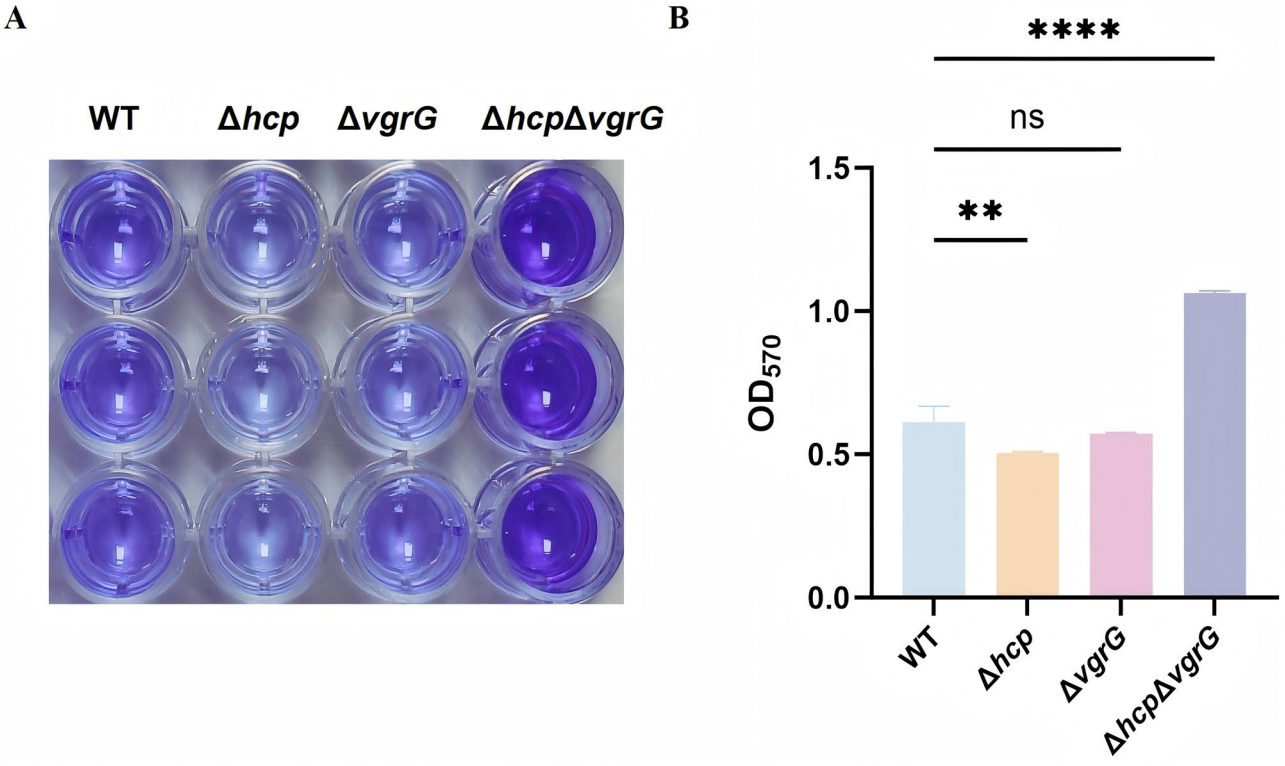

Fig. 6. (**A**) Crystal violet staining of biofilms ($n = 3$); (**B**) The absorbance of biofilm formation was measured at $OD_{570\,nm}$, followed by a one-way ANOVA for statistical analysis. $^{**}p < 0.01$; $^{****}p < 0.0001$; ns, not significant.

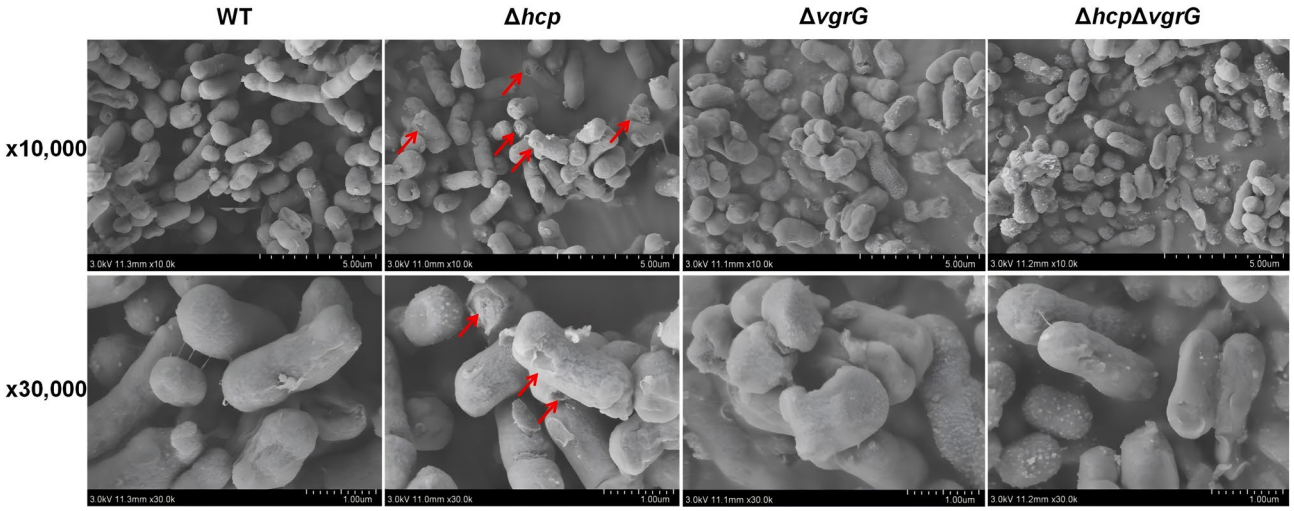

Fig. 7. SEM images of *A. baumannii* at ×10,000 and × 30,000 magnifications. Arrows highlight damaged bacterial surfaces.

release of intracellular components into the supernatant during co-culture. This resulted in the main components of the supernatant and cells being highly similar, making it difficult to distinguish them clearly. Therefore, the pathway analysis focused exclusively on the bacterial components.

In the three bacterial component comparison groups, five statistically significant common differential metabolic pathways were identified. Among these, PTS exhibited significant statistical differences in ATCC17978Δ*hcp*, ATCC17978Δ*vgrG*, and ATCC17978Δ*hcp*Δ*vgrG* ($p = 0.01$, $p = 0.04$, $p = 0.03$). However, in ATCC17978Δ*vgrG*, no significant change in overall PTS expression was observed, which may be attributed to the upregulated NAG-6P expression coupled with downregulated β-Glucoside expression.

The PTS is a unique and complex system in bacteria, which generally includes the histidine phosphocarrier protein (HPr), enzyme I (EI), and a variable number of sugar-specific enzyme II complexes (EIIA, EIIB, EIIC, EIID) that depend on the species[30]. It primarily facilitates the phosphorylation of different sugars and their derivatives via a phosphorelay cascade, subsequently transporting them into the interior of the cell. In addition, PTS is involved in several physiological functions, including central bacterial carbon and nitrogen metabolism[31], virulence regulation[32], stress response mediation[33], biofilm formation[34] and antibiotic resistance[35]thus playing a key role in the overall regulation of bacterial metabolism. Among these functions, PTS is critical for bacterial biofilm formation. For example, in *Streptococcus mutans*, deletion of the *manL* gene, which encodes $EIIAB^{Man}$ in the mannose PTS, leads to impaired PTS function and severely hinders biofilm formation. Similarly, in *Bacillus cereus*, deletion of the *ptsH* gene, which encodes HPr, also impairs PTS function and disrupts biofilm formation[36,37]. Studies on *Vibrio cholerae* have demonstrated that PTS participates in biofilm formation through multiple independent pathways[38].

We conducted systematic phenotypic analyses of four *A. baumannii* strains after co-culture, including biofilm assays, SEM observations, adhesion assays, as well as biofilm-related gene expression detection. Comparative analysis with the wild-type strain revealed distinct phenotypic and genotypic alterations in the mutant strains. The results showed that compared to the wild-type strain, ATCC17978Δ*hcp* exhibited significantly reduced biofilm formation capacity and adhesion ability, while ATCC17978Δ*vgrG* only showed decreased adhesion with no significant difference in biofilm formation. Notably, ATCC17978Δ*hcp*Δ*vgrG* demonstrated enhanced biofilm formation but reduced adhesion ability relative to the wild-type. SEM observations further revealed surface damage in ATCC17978Δ*hcp*, whereas both ATCC17978Δ*vgrG* and ATCC17978Δ*hcp*Δ*vgrG* maintained bacterial surface structure integrity comparable to the wild-type. At the gene relative expression level, RT-qPCR analysis detected upregulation of all examined biofilm-related genes in the double mutant, while only the *csuA* gene showed increased expression in ATCC17978Δ*vgrG* among the single mutants.

These results demonstrate that while there is indeed a correlation between bacterial biofilm formation capacity and adhesion ability, the adhesion ability is not entirely determined by biofilm-forming capability. The integrity of bacterial surfaces and the production of EPS play a crucial role in biofilm formation. Moreover, the expression levels of genes associated with biofilm formation are consistent with the biofilm-forming capacity.

Our research team previously conducted a study on ATCC17978Δ*hcp* and found that its ability to form biofilms was diminished compared to the wild-type strain. However, the biofilm formation ability was restored in the *hcp* complemented strain[39]. Existing literature also supports that *vgrG* deletion does not significantly impact *A. baumannii* biofilm formation, which aligns with our current observations[40]. Surprisingly, ATCC17978Δ*hcp*Δ*vgrG* double mutant displayed a unique phenotypic reversal: significantly enhanced biofilm formation coupled with coordinated upregulation of biofilm-associated genes.

The formation mechanism of bacterial biofilms is highly complex. These results demonstrate that while the PTS influences biofilm formation, it does not serve as the sole regulatory mechanism. The significant changes in the PTS may also influence other phenotypic alterations in bacteria. We hypothesize that dual deletion triggers

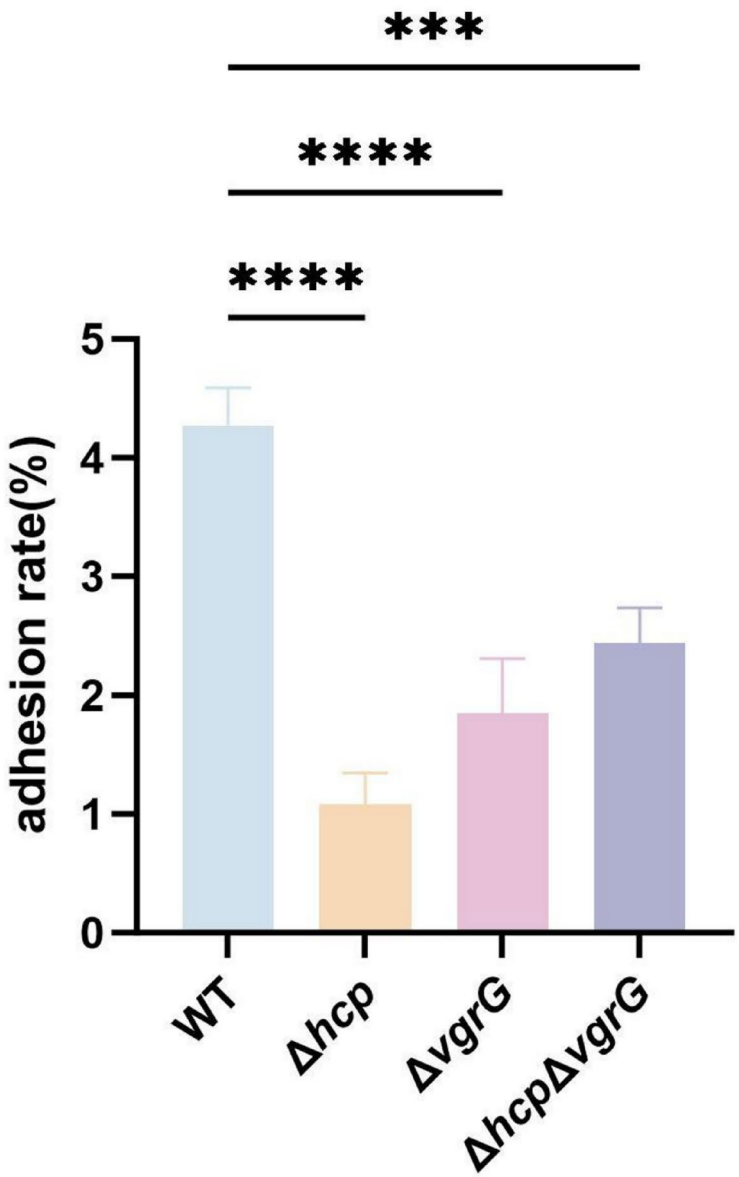

Fig. 8. The rate of bacterial adhesion. Statistical analyses were conducted by one-way ANOVA. ***$p < 0.001$; ****$p < 0.0001$.

specific stress-response pathways as a compensatory survival strategy, ultimately leading to reinforced biofilm production. However, this hypothesis still requires further experimental validation.

Conclusion

The *hcp* gene plays a key role in biofilm formation, while the *vgrG* gene has a comparatively minor impact. The simultaneous absence of both the *hcp* and *vgrG* genes unexpectedly significantly promotes the formation of biofilms.

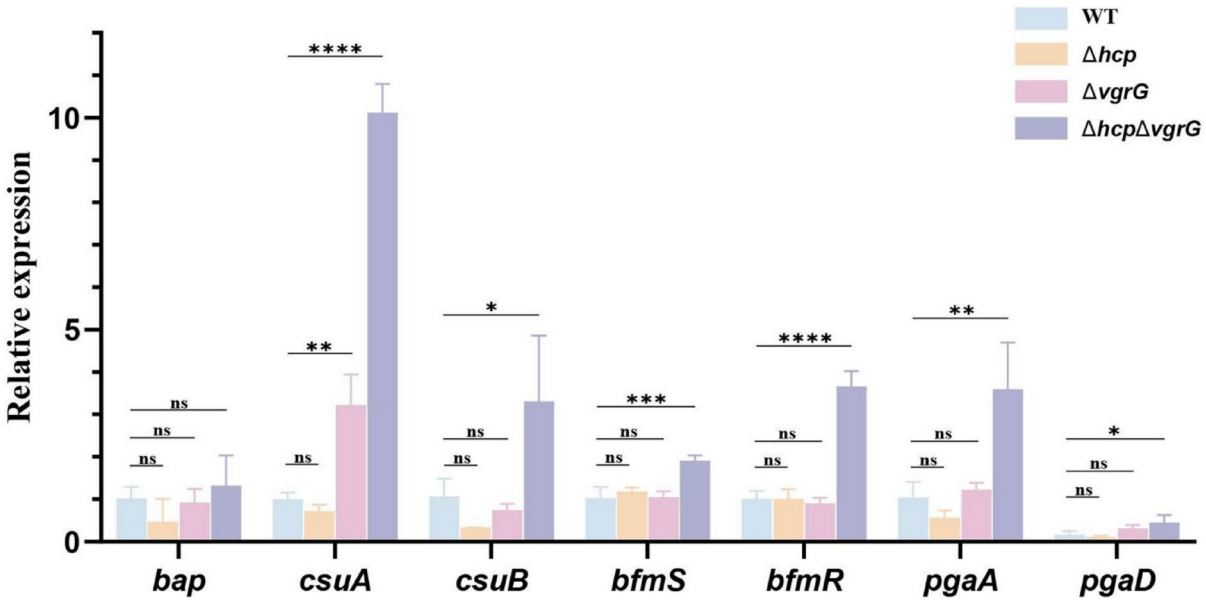

Fig. 9. Relative expression levels of biofilm-associated genes. Statistical analyses were conducted by one-way ANOVA. $^{*}p < 0.05$; $^{**}p < 0.01$; $^{***}p < 0.001$; $^{****}p < 0.0001$; ns, not significant.

Data availability

All original data of this article can be obtained from the corresponding author upon reasonable request.

Received: 24 January 2025; Accepted: 1 September 2025
Published online: 03 October 2025

References

1. Mea, H. J., Yong, P. V. C. & Wong, E. H. An overview of acinetobacter baumannii pathogenesis: motility, adherence and biofilm formation. *MIcrobiol. Res.* **247**, 126722 (2021).
2. Scribano, D. et al. Acinetobacter baumannii OmpA-like porins: functional characterization of bacterial physiology, antibiotic-resistance, and virulence. *Commun. Biol.* **7**, 948 (2024).
3. Knirel, Y. A. et al. 5,7-Diamino-3,5,7,9-tetradeoxynon-2-ulosonic acids in the capsular polysaccharides of acinetobacter baumannii. *Biochem. Biokhimiia*. **88**, 202 (2023).
4. Shan, W., Kan, J., Cai, X. & Yin, M. Insights into mucoid acinetobacter baumannii: A review of Microbiological characteristics, virulence, and pathogenic mechanisms in a threatening nosocomial pathogen. *MIcrobiol. Res.* **261**, 127057 (2022).
5. Weng, Z. et al. Outer Membrane Vesicles from Acinetobacter baumannii: Biogenesis, Functions, and Vaccine Application. *VACCINES-BASEL* 12 (2023).
6. Artuso, I., Poddar, H., Evans, B. A. & Visca, P. Genomics of acinetobacter baumannii iron uptake. *Microb. Genomics* **9** (2023).
7. Zhang, J. et al. SecReT6 update: a comprehensive resource of bacterial type VI secretion systems. *Sci. China Life Sci.* **66**, 626 (2023).
8. Lucidi, M. et al. Pathogenicity and virulence of acinetobacter baumannii: factors contributing to the fitness in healthcare settings and the infected host. *Virulence* **15**, 2289769 (2024).
9. Hayes, B. K. et al. Structure of a Rhs effector clade domain provides mechanistic insights into type VI secretion system toxin delivery. *Nat. Commun.* **15**, 8709 (2024).
10. Dong, J., Liu, C., Wang, P., Li, L. & Zou, Q. The type VI secretion system in acinetobacter baumannii clinical isolates and its roles in antimicrobial resistance acquisition. *Mcrob. Pathogenesis*. **169**, 105668 (2022).
11. Bongiovanni, T. R. et al. Assembly of a unique membrane complex in type VI secretion systems of bacteroidota. *Nat. Commun.* **15**, 429 (2024).
12. Motta, E. V. S., Lariviere, P. J., Jones, K. R., Song, Y. & Moran, N. A. Type VI secretion systems promote intraspecific competition and host interactions in a bee gut symbiont. *P. Natl . Acad. Sci .USA* (2024).
13. He, W. et al. Structure and assembly of type VI secretion system cargo delivery vehicle. *Cell. Rep.* **42**, 112781 (2023).
14. Jurėnas, D. & Journet, L. Activity, delivery, and diversity of type VI secretion effectors. *Mol. Microbiol.* **115**, 383 (2021).
15. Wang, Y. et al. Bacterial strategies for immune systems - Role of the type VI secretion system. *Int. Immunopharmacol.* **114**, 109550 (2023).
16. Lin, Y. et al. Clinical impact of the type VI secretion system on clinical characteristics, virulence and prognosis of acinetobacter baumannii during bloodstream infection. *Microb. Pathogenesis*. **182**, 106252 (2023).
17. Liang, X. et al. VgrG-dependent effectors and chaperones modulate the assembly of the type VI secretion system. *PLOS Pathog.* **17**, e1010116 (2021).
18. Wang, A. et al. Isoniazid derivatization strategy of carboxyl-containing metabolites for LC-MS/MS-based targeted metabolomics. *Anal. BIoanal Chem.* **415**, 6345 (2023).
19. Depke, T., Thöming, J. G., Kordes, A., Häussler, S. & Brönstrup, M. Untargeted LC-MS Metabolomics Differentiates Between Virulent and Avirulent Clinical Strains of Pseudomonas aeruginosa. *Biomolecules* 10 (2020).
20. Aiosa, N. et al. Metabolomics analysis of bacterial pathogen burkholderia Thailandensis and mammalian host cells in Co-culture. *ACS Infect. Dis.* **8**, 1646 (2022).
21. Leggett, A. et al. Cadaverine is a switch in the lysine degradation pathway in Pseudomonas aeruginosa biofilm identified by untargeted metabolomics. *Front. Cell. Infect. MI.*. **12**, 833269 (2022).

22. Zanella, D. et al. Exploiting targeted and untargeted approaches for the analysis of bacterial metabolites under altered growth conditions. *Anal. Bioanal chem*. **413**, 5321 (2021).
23. Thévenot, E. A., Roux, A., Xu, Y., Ezan, E. & Junot, C. Analysis of the human adult urinary metabolome variations with age, body mass index, and gender by implementing a comprehensive workflow for univariate and OPLS statistical analyses. *J. PROTEOME RES.* **14**, 3322 (2015).
24. Zhao, Z. et al. Identification of hub genes for early detection of bone metastasis in breast cancer. *Front. Endocrinol.* **13**, 1018639 (2022).
25. Wishart, D. S. et al. HMDB 4.0: the human metabolome database for 2018. *Nucl. Acids Res.* **46**, D608 (2018).
26. Kanehisa, M., Sato, Y., Kawashima, M., Furumichi, M. & Tanabe, M. KEGG as a reference resource for gene and protein annotation. *Nucleic Acids Res.* **44**, D457 (2016).
27. Kanehisa, M. & Goto, S. KEGG: Kyoto encyclopedia of genes and genomes. *Nucl. Acids Res.* **28**, 27 (2000).
28. Andersen, J. B., Rybtke, M. & Tolker-Nielsen, T. The dynamics of biofilm development and dispersal should be taken into account when quantifying biofilm via the crystal Violet microtiter plate assay. *BIOFILM* **8**, 100207 (2024).
29. Wang, X. & Zhi, Y. Altered Urinary Metabolomics in Hereditary Angioedema. *Metabolites* 12 (2022).
30. Kim, H. J., Jeong, H. & Lee, S. J. Glucose transport through N-Acetylgalactosamine phosphotransferase system in Escherichia coli C strain. *J. Microbiol. BIotechn.*. **32**, 1047 (2022).
31. Sánchez-Cañizares, C. et al. Global control of bacterial nitrogen and carbon metabolism by a PTS(Ntr)-regulated switch. *P Natl. Acad. Sci. USA*. **117**, 10234 (2020).
32. Bier, N., Hammerstrom, T. G. & Koehler, T. M. Influence of the phosphoenolpyruvate:carbohydrate phosphotransferase system on toxin gene expression and virulence in Bacillus anthracis. *Mol. Microbiol.* **113**, 237 (2020).
33. Zeng, J. et al. A broadly applicable, stress-mediated bacterial death pathway regulated by the phosphotransferase system (PTS) and the cAMP-Crp cascade. *P Natl. Acad. Sci. USA*. **119**, e2118566119 (2022).
34. Kong, X. et al. The maltose transporter subunit IICB of the phosphotransferase system: an important factor for biofilm formation of cronobacter. *Int. J. FOOD MIcrobiol.* **370**, 109517 (2022).
35. Jiang, M. et al. Ampicillin-controlled glucose metabolism manipulates the transition from tolerance to resistance in bacteria. *Sci. Adv.* **9**, eade8582 (2023).
36. Gao, T. et al. The phosphotransferase system gene PtsH plays an important role in MnSOD production, biofilm formation, swarming motility, and root colonization in Bacillus cereus 905. *Res. Microbiol.* **170**, 86 (2019).
37. Abranches, J., Candella, M. M., Wen, Z. T., Baker, H. V. & Burne, R. A. Different roles of EIIABMan and EIIGlc in regulation of energy metabolism, biofilm development, and competence in Streptococcus mutans. *J. Bacteriol.* **188**, 3748 (2006).
38. Houot, L., Chang, S., Pickering, B. S., Absalon, C. & Watnick, P. I. The phosphoenolpyruvate phosphotransferase system regulates vibrio cholerae biofilm formation through multiple independent pathways. *J. Bacteriol.* **192**, 3055 (2010).
39. Pan, P. et al. Effect of hcp iron ion regulation on the interaction between acinetobacter baumannii with human pulmonary alveolar epithelial cells and biofilm formation. *Front. Cell. Infect. MI*. **12**, 761604 (2022).
40. Wang, J. et al. The role of the type VI secretion system VgrG gene in the virulence and antimicrobial resistance of acinetobacter baumannii ATCC 19606. *PLOS ONE*. **13**, e0192288 (2018).

Acknowledgements

I would like to express my sincere gratitude to our research team for their collaboration and valuable exchange of ideas.

Author contributions

M.H. wrote the manuscript and analyzed the data. M. L. and W.Y. conducted experiments. P. Q. curated the data. Y.Z. verified data. D. Y. designed the project, guided the research, reviewed the manuscript, and provided the funds.

Funding

This work was supported by the Research Fund of the National Health Commission of the People's Republic of China (grant number WKJ-ZJ-2514); the Construction Fund of Key Medical Disciplines of Hangzhou (Laboratory Diagnostics, grant number 2025HZZD01); and the Natural Science Foundation of Zhejiang Province (grant number LZ22H190002).

Declarations

Competing interests

The authors declare no competing interests.

Additional information

Supplementary Information The online version contains supplementary material available at https://doi.org/10.1038/s41598-025-18287-1.

Correspondence and requests for materials should be addressed to D.Y.